Chemosphere xxx (xxxx) 143888

Contents lists available at ScienceDirect

Chemosphere

journal homepage: www.elsevier.com/locate/chemosphere

Sustainable photocatalytic degradation of antibiotic norfloxacin using microfibrillated cellulose@ZnO nanocomposites

Ramon Resende Leite [a, *], Renata Colombo [b], Ailton José Moreira [c], Júlia Mendes Farias [a], Fausto Eduardo Bimbi Júnior [d], Juliana Bruzaca Lima [c], Marcos Roberto de Vasconcelos Lanza [d], Hernane da Silva Barud [e], Maria Inês Basso Bernardi [a, **]

[a] Sao Carlos Institute of Physics, University of Sao Paulo, 13563-120, Sao Carlos, SP, Brazil
[b] School of Arts, Sciences and Humanities, University of Sao Paulo, 03828-000, Sao Paulo, SP, Brazil
[c] Institute of Chemistry, Sao Paulo State University (UNESP), 14800-060, Araraquara, SP, Brazil
[d] Sao Carlos Institute of Chemistry, University of Sao Paulo, 13560-970, Sao Carlos, SP, Brazil
[e] Biopolymers and Biomaterials Laboratory (BioPolMat), University of Araraquara, 14801-320, Araraquara, SP, Brazil

HIGHLIGHTS

- The study addresses degrading norfloxacin, which poses environmental and health risks.
- Development of highly efficient MFC@ZnO hybrids for NOR photocatalytic degradation.
- Assessment of NOR degradation efficiency under different radiation sources.
- The developed photocatalysts exhibited NOR degradation efficiency exceeding 99%.

GRAPHICAL ABSTRACT

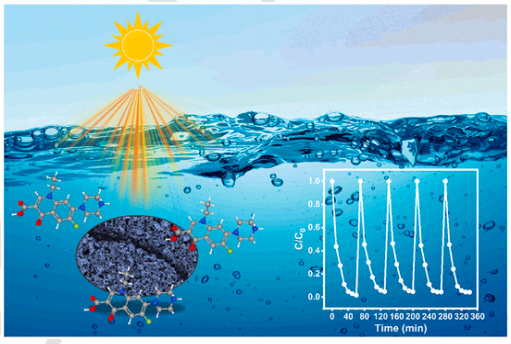

ARTICLE INFO

Keywords:
ZnO/Cellulose composite
Green synthesis of photocatalysts
Fluoroquinolones
Norfloxacin
Antibiotics photocatalytic degradation

ABSTRACT

Antibiotics from the fluoroquinolone class, such as norfloxacin (NOR), are emerging contaminants with significant environmental and human health impacts. Their safe degradation from water remains a global challenge due to their persistence, lack of biodegradability, and ability to induce resistant bacteria. To the best of our knowledge, for the first time, this work reports the development of highly efficient photocatalytic degradation of NOR using environmentally friendly microfibrillated cellulose@ZnO (MFC@ZnO) photocatalysts. Immobilization of ZnO nanoparticles on MFC has played a crucial role in controlling the particle dimensions of ZnO, keeping them around tens of nanometers. The impact of radiation (UV-A, UV-C, and simulated solar light) on NOR degradation efficiency was investigated. Additionally, the effects of catalyst dosage (0.125–0.5 g L^{-1}), NOR concentration (5–20 mg L^{-1}), and degradation pH (pH = 5 to 10) were investigated. LC-MS was used to identify degradation intermediates. The results showed over 94% degradation in 40 min via UV–Vis and 90% in 10 min via HPLC, and recyclability tests indicated MFC0.1@ZnO composites can maintain over 95% NOR degradation efficiency after five consecutive 60-min cycles. The highest NOR degradation efficiency was achieved in a significantly re-

* Corresponding author.
** Corresponding author.
E-mail addresses: ramon.rleite@usp.br (R.R. Leite), m.basso@ifsc.usp.br (M.I. Basso Bernardi).

https://doi.org/10.1016/j.chemosphere.2024.143888
Received 30 April 2024; Received in revised form 24 November 2024; Accepted 2 December 2024
0045-6535/

duced time among metal oxide semiconductors (MOS)-based photocatalysts, thus opening new perspectives for the development of eco-friendly photocatalysts, especially towards emerging pollutant degradation.

1. Introduction

Comprised water quality is one of the main issues of the 21st century as it is estimated that 1.6 million annual deaths are related to contaminated water consumption, corresponding to at least 3900 children per day in developing countries (Martins et al., 2022). The presence of emerging contaminants in environmental ecosystems has been one of the main contamination problems due to environmental risk, adverse effects on aquatic organisms, and plants, as well as contributing to bacterial genotoxicity (AL Falahi et al., 2022; Martins et al., 2022). Therefore, new technologies and processes for the degradation of persistent organic compounds must be developed.

Advanced oxidation processes (AOPs) based on heterogeneous photocatalysis have been recently recognized as a successful solution to the degradation of persistent organic pollutants (Malekkiani et al., 2022; Shen et al., 2022). TiO_2, ZnO, Fe_2O_3, and CuO are some semiconductor oxide materials traditionally used for that purpose (Bano et al., 2023), among which ZnO nanoparticles have been widely adopted due to their excellent photocatalytic properties (Yan et al., 2023a). ZnO, a n-type semiconductor, exhibits high reactivity, photosensitivity, and the ability to generate oxidizing species such as hydroxyl and superoxide radicals (El Golli et al., 2021). It is also chemically, thermally stable, and non-toxic, demonstrating excellent environmental compatibility.

The immobilization of a semiconductor in a biopolymer offers advantages such as reduced costs, high adsorption capacity, high catalytic activity, and great potential for reuse (Du et al., 2018). For example, ZnO/ZnS immobilized in biochar degraded norfloxacin (NOR) by 95% due to the synergy between adsorption and photocatalysis processes (Liu et al., 2020). In another study, ZnO–$Ti_3C_2T_X$ (Z-T) was incorporated into polyacrylic acid/chitosan (PAA-CS) hydrogels to degrade 90% NOR (Chen et al., 2024). Despite the promising results, both studies demonstrated the need for considerable time to achieve high photocatalytic activity in degrading the target pollutant.

Cellulose, an abundant renewable resource, can be an alternative material for immobilizing nanoparticles (Zhang et al., 2021; Qiu et al., 2022). Their high surface area can provide a large substrate for the uniform nucleation and growth of nanoparticles (Das et al., 2022) and their use as substrates for immobilizing nanoparticles. Different studies have focused on the degradation of organic dyes such as methylene blue (Dehghani et al., 2020), rhodamine B (Fu et al., 2017), and methyl orange (Li et al., 2021b) using cellulose-ZnO composite materials. However, the antibiotic degradation from cellulose-ZnO composites is relatively recent (Anirudhan and Deepa, 2017; Tavker and Sharma, 2018; Xiao et al., 2018; Nahi et al., 2021; Yu et al., 2023).

To the best of our knowledge, the first study dates back to 2017, when a ternary composite of zinc oxide-incorporated graphene oxide/nanocellulose (ZnO-GO/NC) was used for the ciprofloxacin photocatalysis, achieving 98% efficiency in 120 min (Anirudhan and Deepa, 2017). Due to the numerous reports of environmental contamination by pharmaceuticals, new degradation technologies based on cellulose-ZnO composites are an important advance in environmental research. Norfloxacin (NOR) is a contaminant resistant to oxidation and of widespread prevalence in aquatic environments. It can be remediated using advanced oxidation technologies (Ding et al., 2017; Yang et al., 2019).

In this study, for the first time, it is proposed to develop eco-friendly photocatalysts comprising ZnO immobilized on MFC for NOR photocatalytic degradation. The photocatalysts were produced through a one-step, low-temperature *in situ* hydrothermal growth process and other stages of easy execution. The hydrothermal reaction was conducted in a highly alkaline aqueous medium with a pH of 12, and photocatalytic experiments were performed under different radiations, such as UV-A, UV-C, and simulated solar light (SSL), for NOR degradation. The steps involved in the NOR degradation were investigated in detail using scavenger assays for reactive species and liquid chromatography coupled with mass spectrometry (LC-MS) measurements to elucidate the transformation products (TP).

2. Experimental

2.1. Materials

Microfibrillated cellulose (MFC) from eucalyptus (Eucalyptus grandis) was provided by Suzano S.A. (Brazil). Zinc chloride, $ZnCl_2$ (≥98%), and norfloxacin, $C_{16}H_{18}N_3FO_3$ (HPLC grade, ≥98%) were purchased from Sigma Aldrich (Brazil), and L-ascorbic acid, $C_6H_8O_6$ (99%), was acquired from Sigma Aldrich (USA). Sodium hydroxide pellets, NaOH (97%), and silver nitrate, $AgNO_3$ (99%), were bought from Synth (Brazil). Absolute ethanol, C_2H_6O, and ammonium oxalate hydrate, $C_2H_8O_4N_2.H_2O$, were obtained from Êxodo Científica (Brazil), and tert-butanol, $C_4H_{10}O$, was purchased from Neon (Brazil). All reagents were of analytical grade and were used without further purification.

2.2. Synthesis of MFC0.1–0.4@ZnO nanocomposites

MFC0.1–0.4@ZnO nanocomposites were obtained through the *in situ* growth of ZnO nanostructures on microfibrillated cellulose (MFC). As in typical procedures, 0.05 mol L^{-1} $ZnCl_2$ aqueous solutions were added dropwise with vigorous stirring to MFC suspensions (0.1, 0.2, and 0.4 wt%). The pH of each mixture was controlled by a dropwise addition of a 0.5 mol L^{-1} NaOH solution under constant stirring until reaching pH = 12. After pH adjustment, each mixture obtained was transferred to individual autoclavable polypropylene screw-capped laboratory bottles, and a hydrothermal treatment was applied at 110 °C for 4 h. The precipitate formed was centrifuged and repeatedly washed with ethanol and distilled water until the pH was 7. The resulting MFC0.1–0.4@ZnO nanocomposites were dried by freeze drying to preserve the frozen structure. The samples were called MFC0.1–0.4@ZnO to distinguish the effect of the concentration of the MFC suspension used in the synthesis of the nanocomposite.

2.3. Characterization of MFC0.1–0.4@ZnO nanocomposites

The crystalline structure of MFC0.1–0.4@ZnO composites was determined by X-ray diffraction (XRD) on a diffractometer (Rigaku Ultima IV, Japan) with Cu-Kα monochromatic radiation (λ = 1.54056 Å). Diffracted intensities were recorded over the 2θ range of 10–80° with a step size of 0.02° and an exposure time of 3 s per step. The morphological analysis was conducted using a field emission scanning electron microscope (FESEM, SUPRA™35, Carl Zeiss, Germany) operating at 5 kV and a transmission electron microscope (TEM, FEI TECNAI G^2 F20, USA) operating at 200 kV. The chemical composition of MFC and nanocomposites was investigated by Fourier-transform infrared spectroscopy (FTIR, Bruker VERTEX 70v, USA), and KBr pellets were prepared at a 1:100 sample/KBr mass ratio for FTIR analysis. FTIR spectra were collected in transmission mode over a 400 to 4000 cm^{-1} range with a 2 cm^{-1} spectral resolution averaging 64 scans. The data processing step normalized the original transmittance (%) results. Optical properties were studied by UV–Vis Diffuse Reflectance Spectroscopy (UV–Vis DRS) on a UV–Vis spectrophotometer (Shimadzu UV-2600i, Japan) equipped with an integrating sphere ($BaSO_4$ as a reference) over a 220–800 nm range. A specific surface area (SSA) analysis determined N_2 adsorption-desorption isotherms at 77 K in a Micromeritics ASAP

2020 analyzer (USA). Before the analysis, the samples were degassed under a vacuum at 70 °C for 24 h to remove moisture. SSA was determined by the multipoint Brunauer-Emmett-Teller (BET) method at a 0 to 1.0 relative pressure (P/P_0). Elemental composition and chemical state of the samples were confirmed by X-ray photoelectron spectroscopy (XPS, Scienta-Omicron ESCA +) with an Al Kα monochromatic X-ray source (hν = 1486.6 eV). XPS spectra were processed by CasaXPS software and calibrated for adventitious carbon energy (284.8 eV).

2.4. Photocatalytic experiments

2.4.1. NOR photodegradation

The NOR photocatalytic degradation was investigated under different radiations, namely, UV-A light (six lamps of 15W F15T8/BL blacklight lamp, Sylvania, Germany), UV-C light (six lamps of 15 W PURITEC HNS Germicidal lamp, OSRAM, Germany), and simulated solar light (one lamp of Ultra Vitalux 300 W, OSRAM, Germany). The emission spectra of each lamp used are shown in Fig. S1. These spectra were obtained using an SPR-01 spectroradiometer (Luzchem), which determined the maximum excitation wavelength of the samples. Typically, 12.5 mg of MFC0.1–0.4@ZnO photocatalysts were dispersed in NOR aqueous solutions (50 mL, 5 mg L^{-1}), and the suspensions were vigorously stirred for 60 min in the dark towards adsorption-desorption equilibrium between the photocatalyst and the pollutant. After irradiation, a 1.5 mL aliquot was sampled every 10 min, and the supernatant was collected by centrifugation and filtered in a syringe filter comprising PVDF membrane (0.22 μm pore size and 25 mm diameter). NOR photodegradation efficiency was initially monitored by a change in maximum absorbance at λ = 273 nm in a UV–Vis spectrophotometer (Kasuaki IL-593). The effects of catalyst dosage (0.125, 0.25, and 0.5 g L^{-1}), NOR concentration (5, 10, and 20 mg L^{-1}), and solution pH (5, 7.6, and 10) were also investigated. The pH adjustment was performed using 0.1 mol L^{-1} HCl and 0.05 mol L^{-1} NaOH solutions.

The analytical curve for NOR concentration analysis was constructed in the 0.5–6.5 mg L^{-1} range. A high-performance liquid chromatography with a UV-DAD detector (Shimadzu Prominence HPLC model LC-20AT) and a C18 column (Phenomenex®, 150 mm length; 4.6 mm diameter; 5 μm particle size) was used for separation. In isocratic elution mode, the mobile phase consisted of 0.1% ($v{\cdot}v^{-1}$) formic acid and acetonitrile at a 70:30 ratio. Injection volume, UV detection wavelength, and column conditioning temperature were 25 μL, 273 nm, and 23 °C, respectively.

Additionally, aliquots collected from the photocatalytic experiments were analyzed by liquid chromatography coupled with mass spectrometry (LC-MS, LC/MS-8030 triple quadrupole, Shimadzu Co., Japan) to determine the transformation products of norfloxacin. The analysis was conducted on a Shim-pack ODS II column (3 mm i.d. × 100 mm, 2.2 μm) at 26 °C. The mobile phase consisted of water (A) and acetonitrile (B), both containing 0.1% formic acid. Elution was carried out at a flow rate of 0.8 mL min^{-1} following a gradient program: 0–5 min: 10–37% (B); 5–8 min: 37–100% (B); and 8–10 min: 100–10% (B). The electrospray interface (ESI) operated in positive ionization mode at 400 °C and 4.5 kV. Full-scan spectra were acquired in a positive ion mode over an m/z range from 100 to 500. Nitrogen served as both the nebulizer and desolvation gas, with flow rates of 3 and 15 L min^{-1}, respectively.

Tert-butanol (t-BuOH), ammonium oxalate (AO), ascorbic acid (AA), and silver nitrate ($AgNO_3$) were used as scavengers of $HO^{\bullet}$, h^+, $O_2^{\bullet-}$, and e^-, respectively (Lima et al., 2021).

2.4.2. Recyclability studies

Recyclability experiments were conducted for the MFC0.1@ZnO sample. Five consecutive cycles were performed under simulated solar light and constant photocatalysis conditions. After each cycle, the catalyst was recovered through centrifugation, successively washed in ethanol and distilled water for elution of residual impurities, and then lyophilized.

A high-resolution molecular absorption spectrometer (HR-CS MAS ContrAA 300 model, Analytik Jena, Jena, Germany) was utilized for the quantification of Zn^{2+} in lixiviate samples post-photocatalysis (2 h). The limit of detection (LOD) was determined to be 1.6 mg L^{-1}, while the limit of quantification (LOQ) was 5.3 mg L^{-1}. The calibration curve showed a linear adjustment coefficient (R^2) of 0.961. Moreover, Zn^{2+} was monitored at a wavelength of 213 nm, with a linear range established between 1 and 7 mg L^{-1}, based on previous Zn^{2+} concentration analyses in the samples.

2.4.3. Phytotoxicity methodology

A phytotoxicity assay using *Cucumis sativus* seeds was conducted on samples before and after the degradation assays. The analysis was performed in triplicate across four groups: control (double-distilled water), NOR solution, photolysis, and photocatalysis (MFC0.1@ZnO). Initially, the seeds were washed with a 4% ($v{\cdot}v^{-1}$) sodium hypochlorite solution and dried at room temperature. For each experimental group, 10 seeds were placed in Petri dishes lined with filter paper (90 mm × 80 g/m^2). Five milliliters of the respective contaminant or control solutions were then added to the filter paper. The Petri dishes were incubated in the dark at 25 ± 2 °C for 5 days. The germination index (GI) and relative root growth rate (RGI) of *C. sativus* were calculated using the following equations:

$$\mathrm{GI}\ (\%) = \frac{NGS}{NGC}\ \mathrm{x}\ 100 \qquad \text{Eq. 01}$$

$$\mathrm{RGI}\ (\%) = \frac{RLS}{RLC}\ \mathrm{x}\ 100 \qquad \text{Eq. 02}$$

where RLS and RLC represent the relative length of the roots (RLS) of the groups and the control (RLC), respectively. In addition, the germination index (GI) is calculated as the ratio of the number of germinated seeds in the treated samples (NGS) to the number of germinated seeds in the control (NGC). The data was presented based on the mean and standard deviation of the triplicate values obtained.

3. Results and discussion

3.1. XRD analysis

The XRD results of MFC0.1–0.4@ZnO nanocomposites are shown in Fig. 1a. The peaks centered at 16.4° and 22.5° are characteristic of type I cellulose (Yan et al., 2023b) and were identified in all nanocomposites. The peaks identified in 2θ = 31.6°, 34.3°, 36.2°, 47.4°, 56.5°, 62.8°, 67.8°, and 69.0° were indexed to the crystallographic planes (100), (002), (101), (102), (110), (103), (112), and (201) of the hexagonal wurtzite crystal structure of ZnO (JCPDS no. 36–1451), respectively (Pinheiro et al., 2020; Li et al., 2023; Shi et al., 2023). This result highlights the successful *in situ* immobilization of ZnO NPs on MFC during hydrothermal growth. A dominant peak at 36.2° was observed in the XRD patterns of the composites. As the MFC concentration increased in the composites, the cellulose diffraction peaks became more prominent in the diffractograms. Interestingly, the non-polar (100) and polar (002) planes maintained similar intensities regardless of the MFC concentration used in the composite synthesis (Silva et al., 2023). The intensity ratio between those planes may indicate facet exposure (Jing et al., 2022), and a high I(002)/I(100) ratio suggests preferential growth along the polar c-axis (Singh et al., 2019; Li et al., 2022). Conversely, a ratio close to unity suggests isotropic growth, i.e., no preferential direction of ZnO NP growth on the MFC surface. The absence of secondary peaks results in the formation of high-purity MFC0.1–0.4@ZnO composites, and the diffraction peaks relative to ZnO in the composites are

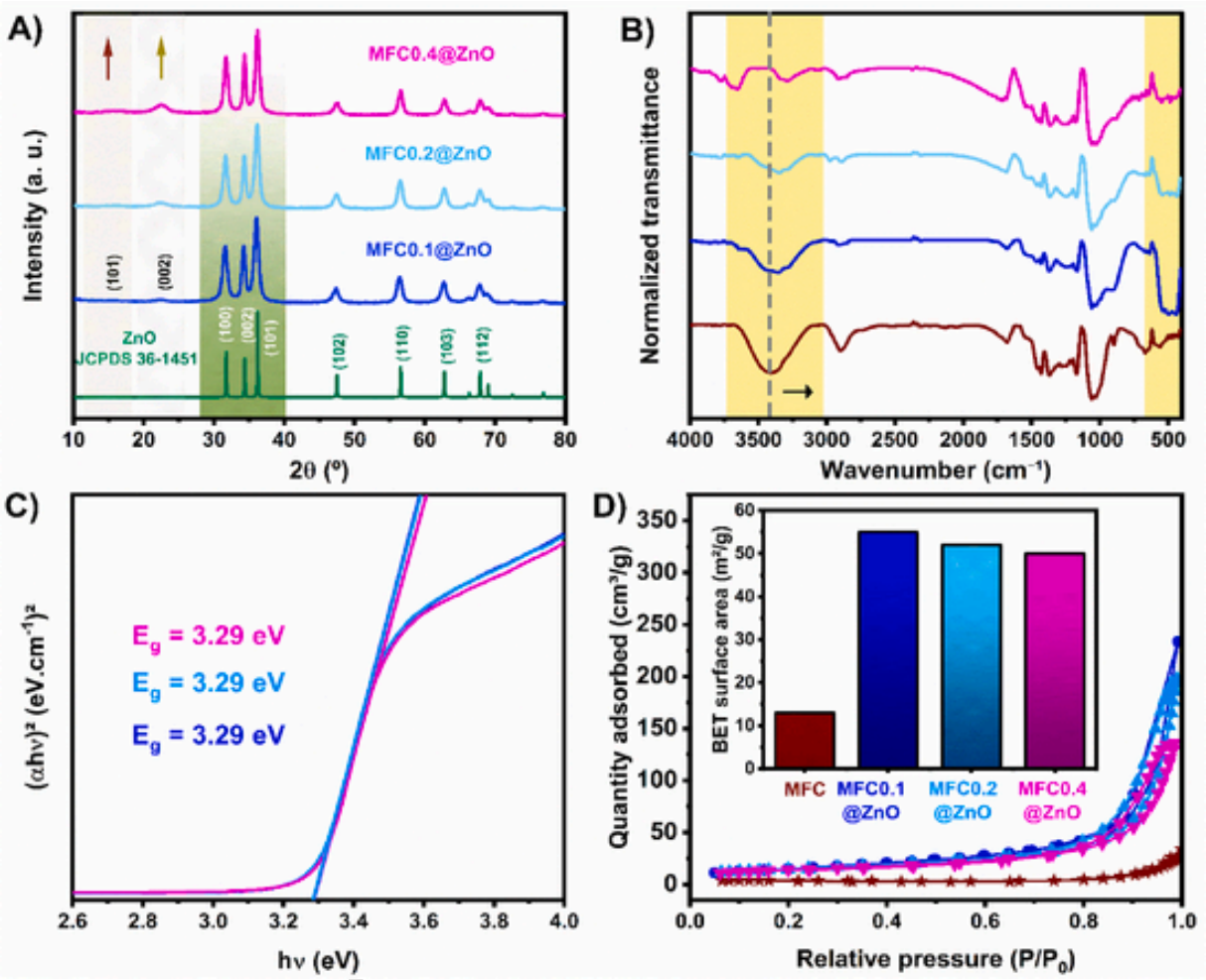

Fig. 1. (a) XRD patterns; (b) FTIR spectra; (c) estimation of the band gap by Tauc plot; and (d) BET surface area of MFC and MFC0.1–0.4@ZnO nanocomposites.

relatively broad, indicating a homogeneous distribution of ZnO crystals in the cellulose matrix, which inhibits crystallite growth.

3.2. FTIR characterization

The chemical structure of MFC0.1–0.4@ZnO nanocomposites was analyzed by FTIR spectroscopy, and the normalized spectra are shown in Fig. 1b. Bands centered at 2896, 1640, 1430, 1026 and 896 cm^{-1}, associated with vibrations of aliphatic C–H groups, stretching of C═O groups, CH_2 bending, C–O vibration and β-glycosidic bonds between glucose units in cellulose and general structure, respectively (Tan et al., 2018; Chen et al., 2023; Vasistha et al., 2023) were observed in both MFC and nanocomposites. Compared to MFC, new bands in the 400 to 600 cm^{-1} range were identified in the nanocomposites, with bands at 422 and 579 cm^{-1} attributed to the stretching of Zn–O single bonds (Li et al., 2023). The shift to lower wavenumbers of MFC hydroxyl group vibrations in the composites suggests a strong hydrogen bonding interaction with ZnO (Li et al., 2021a). The positions of the hydroxyl groups in MFC, MC0.1@ZnO, MFC0.2@ZnO, and MFC0.4@ZnO were found to be 3408, 3377, 3350, and 3292 cm^{-1}, respectively. Additionally, the reduction in the intensity of oxo-functional bands indicates the hydroxyl groups are occupied with ZnO (Ko et al., 2014).

3.3. Optical properties: UV–Vis diffuse absorption spectroscopy

The optical properties of composites were measured by UV–Vis DRS, and the results are shown in Fig. 1c. The band gap energy (E_g) was determined from the absorption spectrum by the Tauc equation:

$$(\alpha h\nu)^2 = A(h\nu - E_g) \quad \text{Eq. 03}$$

where α represents the absorption coefficient, A is a constant, and hν denotes photon energy. The E_g value was determined by extrapolating the linear portion of the curves from the graph of $(\alpha h\nu)^2$ versus hν. The E_g = 3.29 eV remained unchanged as the concentration of MFC suspension increased in the composite formulation (Fig. 1c). Although E_g depends on various factors such as chemical composition, crystal structure, crystallinity, particle size, and morphology (Arakha et al., 2017; Agarwal et al., 2019), the uniform distribution of ZnO nanogranules in the cellulose matrix did not significantly affect them.

3.4. Brunauer-Emmett-Teller (BET) surface area analysis

The N_2 adsorption-desorption isotherms of MFC0.1–0.4@ZnO composites exhibited a type IV pattern, accompanied by an H3 hysteresis loop due to the capillary condensation (Mohamed et al., 2016), thus indicating the presence of material with mesoporous characteristics (Zhao et al., 2022) (Fig. 1d). The specific surface areas (SSA) of MFC and MFC0.1@ZnO, MFC0.2@ZnO, and MFC0.4@ZnO composites cal-

culated by the Brunauer-Emmett-Teller (BET) multipoint method were 13, 55, 52, and 50 m^2/g, respectively. The SSA of the composite materials was not significantly altered, possibly due to the extremely reduced particle size resulting from the immobilization of ZnO NPs on cellulose fibers. As illustrated in the FE-SEM images, no statistical difference in the average particle size was observed.

Regarding MFC, the increase in SSA observed in the composites can be attributed to the loading of ZnO (Yan et al., 2023b). This phenomenon arises due to the affinity of ZnO, an amphoteric substance, for establishing stronger hydrogen bonds with cellulose molecules compared to hydrated NaOH (Kamal Mohamed et al., 2015). During hydrothermal growth under high alkaline conditions, zincate growth units, $Zn(OH)_4^{2-}$, can establish new hydrogen bonds with cellulose, thus breaking intermolecular hydrogen bonds between cellulose chains. These additional hydrogen bonds facilitate the dispersion of microfibrillated cellulose and a more efficient separation, thereby increasing the effective surface area. The increased steric hindrance caused by the introduction of $Zn(OH)_4^{2-}$ keeps the cellulose chains further apart, minimizing the aggregation of microfibrillated cellulose. This leads to a more uniform distribution in the composite, contributing to the increase in the specific surface area. According to Dehghani et al. (2020), the photocatalytic reaction between the catalyst and organic compounds occurs mainly on the catalyst surface (Dehghani et al., 2020). Therefore, a high surface area of the catalyst tends to enhance the photocatalytic performance.

3.5. Morphology analysis

Fig. 2 displays the microstructures of MFC0.1–0.4@ZnO nanocomposites. With a lower mass ratio of MFC suspension, 0.1% wt, microfibrillated cellulose was coated with ZnO nanogranules measuring tens of nanometers (Fig. 2a). Increasing the concentration of MFC suspension to 0.2% wt resulted in a higher quantity of MFC in the composite, yet the shape of the immobilized ZnO NPs within the MFC network remained unchanged (Fig. 2b). Upon increasing to a 0.4% wt MFC formulation, the three-dimensional structure of the cellulose fibril network was observed, and ZnO NPs were anchored and grown *in situ* on the surface and in the spaces between MFC (Fig. 2c). Bright-field (BF) TEM images of the nanocomposites were used to measure their size (Fig. 2d–f). The distribution of the average size of ZnO NPs remained constant for the different concentrations of MFC suspensions investigated. The distribution and average size of the particles ranged from 20 to 50 nm, with an average diameter of 40 nm. This narrow distribution highlighted the fundamental role of MFC as a support for the uniform and dispersed growth of ZnO NPs on the microfibrils in the evaluated composites.

The three-dimensional structure of MFC and the hydrogen bonding with ZnO NPs promoted a favorable environment for the uniform growth of ZnO. The porous organization of MFC acted as a support for the growth of ZnO particles, wherein the cellulose fibrils provided active sites for nucleation. In turn, the hydrogen bonds provided stability and adhesion at the interface between the materials, ensuring firm anchoring and uniform growth of ZnO NPs on the MFC surface. Furthermore, the three-dimensional structure of the MFC network limited the growth of ZnO particles by controlling the nucleation kinetics and growth process (Hoogendoorn et al., 2022). The presence of the organic matrix reduces the interfacial energy, resulting in a lower barrier to nucleation (Montero-Muñoz et al., 2018), thus favoring efficient nucleation, enabling controlled particle growth, and obtaining smaller sizes compared to conditions with higher interfacial energy (Resende Leite et al., 2024). Cellulose fibers can efficiently complex Zn^{2+} ions and uniformly disperse ZnO NPs due to the synergistic effect of electrostatic adsorption and steric hindrance (Yan et al., 2023b). As a result of isotropic growth, ZnO nanogranules were obtained.

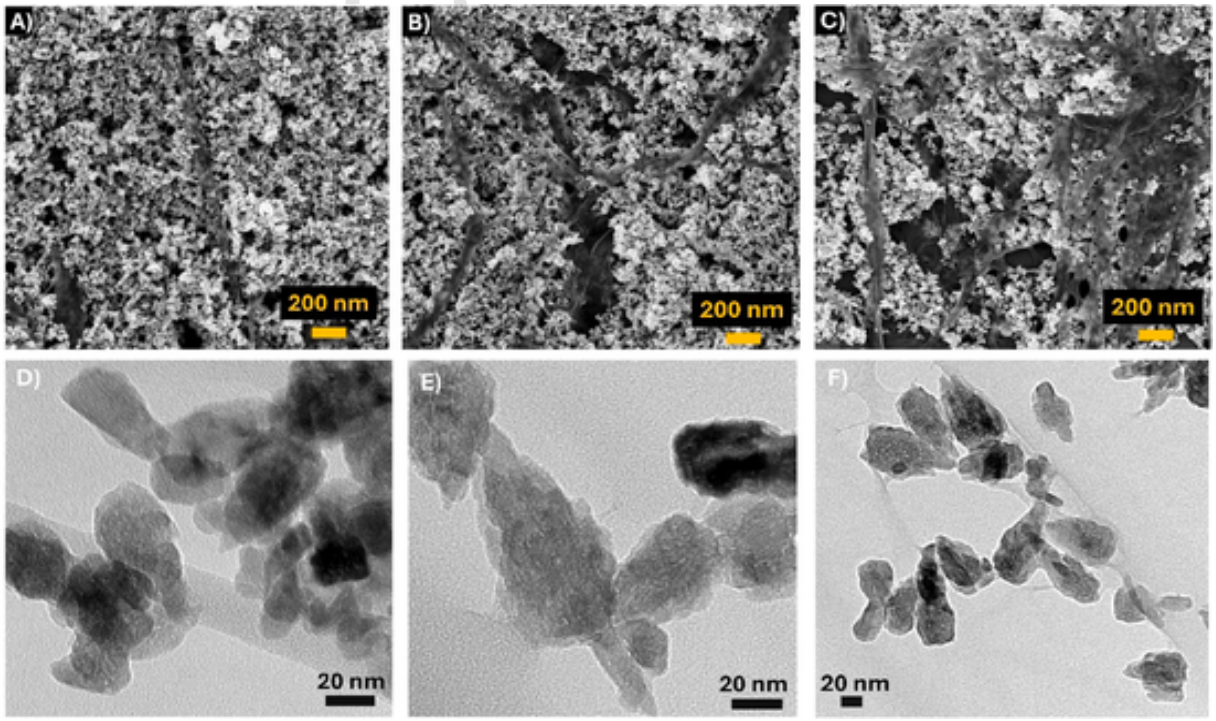

Fig. 2. Morphological characterization of nanocomposites. FEG-SEM images of (a) MFC0.1@ZnO, (b) MFC0.2@ZnO, and (c) MFC0.4@ZnO, respectively. Figures (d)–(f) present the corresponding BF TEM images.

3.6. Mechanism of ZnO NPs formation on MFC matrix

The formation of ZnO nanogranules on the microfibrillated cellulose (MFC) network involves the following steps:

$$ZnCl_2(aq) \rightarrow Zn^{2+} + 2\ Cl^- \quad R1$$

$$MFC + Zn^{2+} \rightarrow MFC \ldots Zn^{2+} \quad R2$$

$$MFC \ldots Zn^{2+} + 2\ OH^- \rightarrow MFC \ldots Zn(OH)_2 \quad R3$$

$$MFC \ldots Zn(OH)_2 + 2\ OH^- \rightarrow MFC \ldots Zn(OH)_4^{2-} \quad R4$$

$$MFC \ldots Zn(OH)_4^{2-} \rightarrow MFC@ZnO + H_2O + 2\ OH^- \quad R5$$

Initially, $ZnCl_2$ was dissolved in distilled water to produce Zn^{2+} ions. Due to the dropwise addition of the zinc precursor solution to MFC, Zn^{2+} ions were absorbed by the surface of the cellulose fibers and pre-nucleation was initiated by establishing electrostatic interaction between oxygen atoms of hydroxyl and Zn^{2+} (Janpetch et al., 2016; Li et al., 2019). After adding the OH^- ion, a white precipitate of $Zn(OH)_2$ formed, effectively binding to the cellulosic substrate (Song et al., 2024). Upon the NaOH addition to the reaction medium, the high alkalinity resulted in an excess of OH^- ions, which bound to the zinc ions to form primary growth units, $Zn(OH)_4^{2-}$ (Supramaniam et al., 2021). The porous structure of the cellulose matrix played a crucial role in hindering the diffusion of the precursor $[Zn(OH)_4^{2-}]$, enabling more precise control over the growth of ZnO NPs (Fu et al., 2017). Such diffusion hindrance contributed to the formation of a controlled morphology and positively influenced the properties of the composite, as discussed in Section 3.8. During the hydrothermal reaction, the growth units anchored to the surface of the microfibrillated cellulose were subsequently dehydrated to form ZnO NPs.

3.7. XPS analysis

The elemental composition and chemical state of the samples were systematically analyzed using XPS. Fig. 3(a–c) present the survey spectra of the MFC0.1–0.4@ZnO composites, revealing an elemental composition that includes zinc (Zn), carbon (C), and oxygen (O), with no detectable impurities within the limits of the technique. The high-resolution Zn 2p spectra revealed a doublet, with binding energies ranging from 1021.1 to 1021.8 eV for Zn $2p_{3/2}$ and from 1044.2 to 1044.8 eV for Zn $2p_{1/2}$ (Fig. 3d–f), consistent with photoelectron emission from these levels (Li et al., 2021b). Although a slight shift in the Zn 2p components was observed among the composites, the energy difference between the doublets, resulting from spin-orbit coupling, was 23.1 eV, indicating that Zn ions are in the +2 oxidation state. Notably, the immobilization of ZnO nanoparticles on MFC does not alter the oxidation state of ZnO.

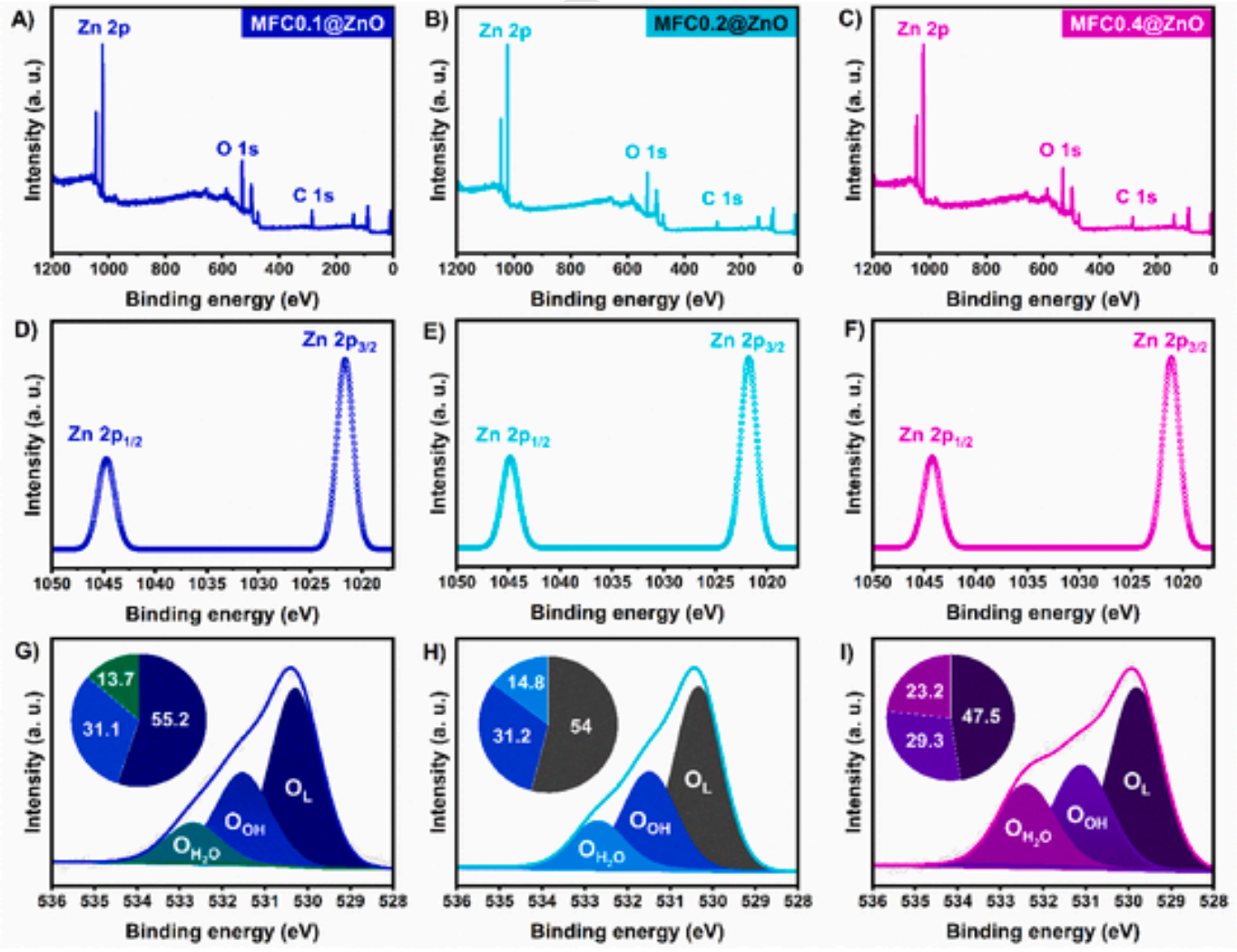

Fig. 3. XPS spectra of MFC0.1–0.4@ZnO composites: (a, b, c) survey, (d, e, f) Zn 2p, and (g, h, i) O 1s.

The high-resolution XPS spectra for O 1s, presented in Fig. 3(g–i), were deconvoluted into three distinct components. The binding energies at 529.8–530.3 eV correspond to lattice oxygen (Li et al., 2021b), while the ranges of 531.1–531.5 eV and 532.4–532.7 eV are attributed to hydroxyl (OH) groups (Zhou et al., 2019; Zhang et al., 2021) and adsorbed water molecules on the photocatalyst surface, respectively. As the concentration of MFC suspension in the composites increased, a slight increase in the concentration of OH groups and a decrease in lattice oxygen were observed. This relationship can be identified from the relative ratio between the integration areas of OH/O_L. The relative ratios between those peaks for MFC0.1@ZnO, MFC0.2@ZnO, and MFC0.4@ZnO were 0.56, 0.58, and 0.61, respectively. Additionally, a shift of the O 1s spectrum components to lower energy was observed with the increase in MFC concentration, which can be attributed to the interaction between the oxo-functional groups present in the cellulose fibrils and the oxygen ions in the ZnO structure. As the MFC concentration increases, more oxo-functional groups are available on the surface of the cellulose fibrils to interact with the oxygen ions in ZnO. The oxo-functional groups can donate electrons to the oxygen ions in the ZnO structure or establish hydrogen bonds with them, resulting in a redistribution of the charge density and, hence, a shift of the O 1s spectrum components to lower energies.

3.8. Photocatalytic activity

Fig. 4(a–c) shows the photocatalytic activity of MFC0.1–0.4@ZnO composites for NOR degradation under different radiations (UV-A, UV-C, and SSL). The NOR removal in the dark is attributed to the adsorption on the photocatalyst surface at 20 min. After adsorption-desorption equilibrium for 20 min, the NOR adsorption for MFC0.1@ZnO, MFC0.2@ZnO, and MFC0.4@ZnO samples was 25.44 ± 0.02%, 22.60 ± 0.03%, and 24.16 ± 0.05%, respectively (Fig. 4a, b, and c). The NOR adsorption capacity of the photocatalysts did not vary significantly with increasing MFC concentrations in the composite formulations due to the saturation tendency of the available interaction sites. Since the specific surface areas of the composites are similar, the availability of active sites for the adsorption process remains constant.

The photocatalytic degradation of NOR using a UV-A lamp (Fig. 4a), UV-C lamp (Fig. 4b), or solar simulator (Fig. 4c) as a light source showed a degradation <25% by photolysis in 60 min. However, the composites applied as a photocatalyst for NOR degradation were very efficient under any of the three radiation sources, achieving >99% NOR degradation in 60 min. These results confirm that the composites are effective photocatalysts for absorbing and converting broad-

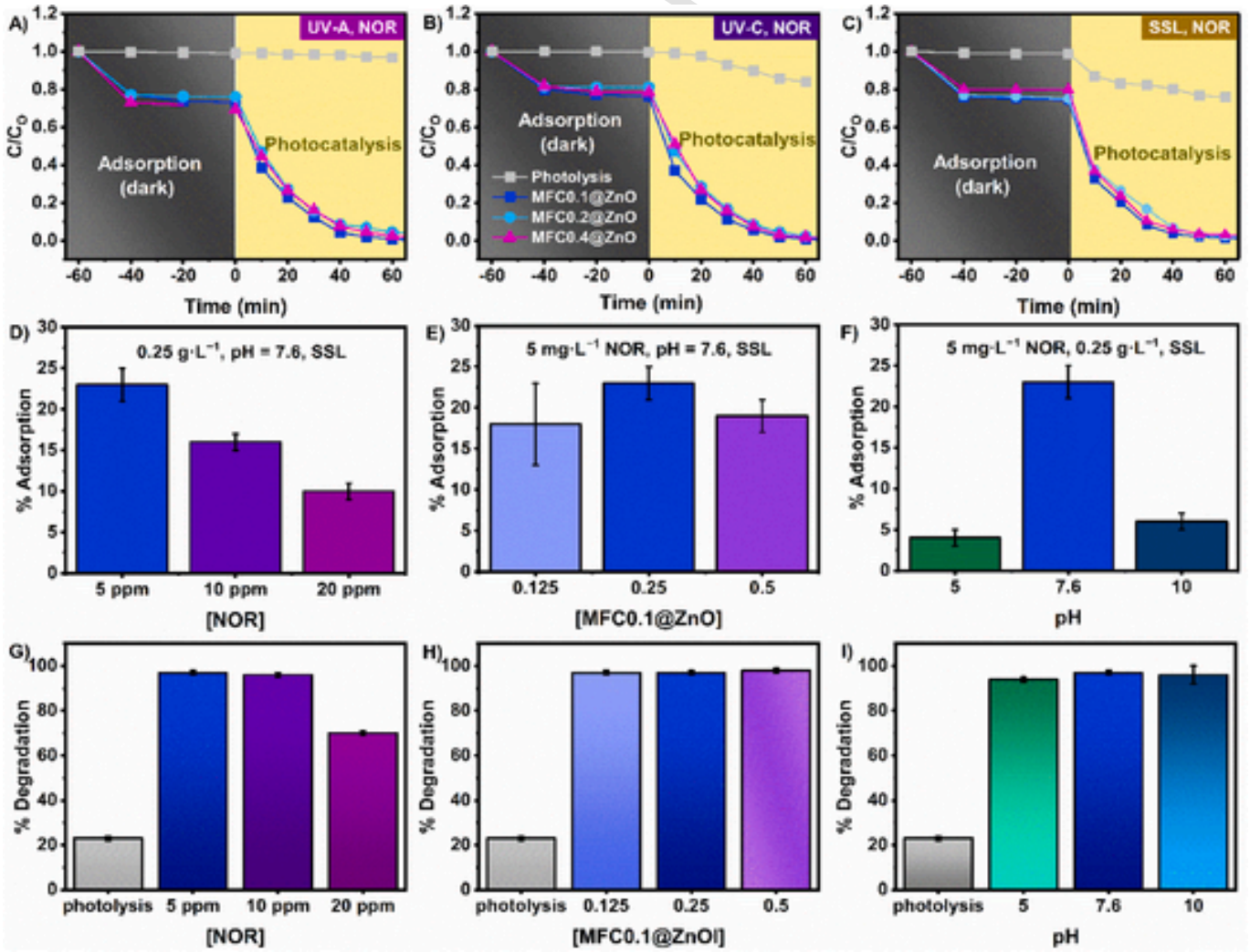

Fig. 4. Photocatalytic experiments with NOR using MFC0.1–0.4@ZnO nanocomposites under different radiations: (a) UV-A light, (b) UV-C light, and (c) simulated solar light (C_O = 5 mg L^{-1} NOR, photocatalytic dosage = 0.25 g L^{-1}, pH = 7.6, and 25 °C) (d) effect of MFC0.1@ZnO dosage, e). NOR concentration, and f) pH on degradation under simulated solar light.

spectrum light energy into processes capable of degrading NOR. Experiments monitored by UV–Vis for MFC0.1@ZnO photocatalyst indicated significant NOR degradation in the first 10 min (Fig. S2), during which the efficiency was higher under simulated sunlight (56.3%), followed by UV-C (51.3%) and UV-A (47.1%). This is because SSL has high-intensity emission and irradiance in the UV-A region, which allows for the photo-activation of the MFC0.1@ZnO photocatalyst (E_g = 3.29 eV). A similar behavior was observed for the other synthesized photocatalysts. However, the characteristic molecular absorption of NOR within the 250–300 nm wavelength range is attributed to $\eta \rightarrow \sigma^*$ transitions, originating from saturated C–N bonds, as well as to $\pi \rightarrow \pi^*$ and $\eta \rightarrow \pi^*$ transitions of chromophores groups, C═C, and aromatic bonds within the quinolone ring (Son et al., 1998). During photocatalysis, the TP formation with chromophore groups similar to those of the target molecule likely generated absorption at the monitored wavelength (273 nm), interfering with the monitoring.

Therefore, the HPLC analyses were performed, and the results also revealed higher degradation efficiency at shorter times (Fig. S2). UV–Vis spectrophotometry is not a good analytical option when the formation of transformation products is expected. This is because spectral bands can overlap in the molecular absorption spectrum obtained after each degradation time. However, the HPLC analysis is highly-sensitive and capable of detecting and quantifying different components, providing a more accurate analysis of the actual NOR concentration and its transformation products (TP) during the photocatalytic reaction. Chromatography is an important technique for separating components, eliminating the problems of spectral interference characteristic of spectrophotometric analyses. Therefore, HPLC can distinguish between the absorption of the target substance (NOR) and possible interferents or TP, ensuring reliable results. Regarding HPLC analysis, the diode array ultraviolet detector (UV-DAD) and the chromatographic conditions enabled an NOR effective separation. Consequently, the target molecule could be quantified with no interference from other detected intermediates. Thus, the discrepancy in degradation values monitored by HPLC and UV–Vis can be attributed to the differences in sensitivity between the two techniques mentioned. Despite the limitations presented, UV–Vis remains the predominant technique for evaluating drug degradation (Kar et al., 2023; Zhao et al., 2023), possibly due to its cost and greater accessibility. The pseudo-first-order kinetic was calculated by Eqs. (4) and (5) from the spectrophotometric and chromatographic data (Fig. S2).

$$dC/dt = -kC \quad \text{Eq. 04}$$

$$-\ln(C_t/C_0) = kt \quad \text{Eq. 05}$$

where C_0, C_t, k, and t denote concentration after adsorption-desorption equilibrium, concentration of NOR at a given time, reaction rate constant, and irradiation time, respectively.

The k values obtained from the spectrophotometric analyses were up to 67% lower than the values obtained from the chromatographic analyses, showing the need for extra care when using spectrophotometric techniques. Whereas chromatographic data is considered more appropriate, the k and R^2 values calculated after photocatalysis with MFC0.1@ZnO were k = 0.131 min^{-1} and R^2 = 0.994 for UV-A, k = 0.151 min^{-1} and R^2 = 0.978 for UV-C, and k = 0.213 min^{-1} and R^2 = 0.999 for SSL light (Fig. S2).

As the kinetic studies achieved the highest k value for the MFC0.1@ZnO catalyst, this was chosen to investigate the influence of NOR concentration, pH, and catalyst dose. The NOR adsorption in 60 min showed a decrease as the concentration increased from 5 to 20 mg L^{-1} (Fig. 4d). This behavior is due to the adsorption sites saturation at higher concentrations, which can impair the photocatalytic activity of the catalyst. The different doses applied (0.125, 0.25, or 0.5 g L^{-1}) fixing the NOR concentration (5 mg L^{-1}) showed no significant difference in NOR adsorption capacity (Fig. 4e). However, as the average adsorption for the 0.25 g L^{-1} dose showed the highest value, this was considered for the conditions of the experiment. The influence of pH on NOR adsorption was significant for the values investigated: pH = 5, 7.6, or 10 (Fig. 4f). The NOR has an acidic pKa = 6.34 and a basic pKa = 8.75 and is protonated at pH < 6.34, deprotonated at pH > 8.75, and neutral between these values (Chen et al., 2021). The adsorption of 23% at pH = 7.6 was much higher than the values of 4 or 6% obtained at pH = 5 or pH = 10, respectively. These results confirm that the interaction between the neutral form of NOR and the catalyst is effective in the application stage, which may favor photocatalytic degradation due to the greater proximity of the contaminant to the photocatalysts.

The photocatalysis results under SSL for different concentrations of NOR, dosages of MFC0.1@ZnO, and pH conditions are presented in Fig. 4g, h, and i, respectively. Since photocatalysis occurs on the surface of the photocatalyst, the condition with the highest adsorption was chosen to determine the optimal catalyst dosage, which was established at 0.25 g L^{-1}. At this stage, photolysis under SSL contributed less to the degradation of NOR (Fig. 4h), whereas the MFC0.1@ZnO photocatalyst achieved NOR degradation >90% for the 5 or 10 mg L^{-1} concentration at all the catalyst doses applied and at all the pH values investigated, as shown in Fig. 4g and i. The pH of effluents containing trace amounts of antibiotics in wastewater typically ranges from neutral to slightly alkaline, in accordance with industrial and hospital effluent disposal guidelines (Manasa et al., 2021), which justifies the choice of degradation at a pH around 8. Additionally, this pH is achieved by dispersing the catalyst in the solution containing NOR, eliminating the need for further pH adjustment and making the photocatalytic process more practical (Leite et al., 2024). This high performance of the photocatalyst in degrading NOR under different application conditions reinforces that this material has great potential for treating effluents containing this molecule without many adjustments to the physical-chemical conditions before application. It is therefore possible to work with high or low concentrations, doses, or pH.

The photocatalysts developed in this study were compared with other materials from the literature (Table 1). A literature review revealed a lack of studies applying photocatalysts comprising semiconductor materials immobilized on carbon substrates and polymeric materials. The synthesis of ZnO nanostructures on microfibrillated cellulose proved advantageous in producing highly effective, eco-friendly photocatalysts for NOR degradation, demonstrating superior performance compared to the investigated materials.

3.9. Radical-trapping experiments by different scavengers

Free radical elimination experiments determined the most important reactive species in the NOR photocatalytic degradation process (Fig. 5a). The AA addition decreased the NOR degradation efficiency, significantly reducing activity from 98.4% to 54.2%. The t-BuOH addition also highlighted the importance of $HO^{\bullet}$ in the photocatalytic process, with a 33.9% decrease in photocatalytic performance. However, the NOR photodegradation efficacy was slightly reduced with the $AgNO_3$ addition, suggesting electrons have a limited influence on the overall photocatalytic process. The scavenger results suggest a lower recombination of the electron-hole pair, indicating that e^- and h^+ have a slight effect on the reaction (Leite et al., 2024). The photocatalysis reaction for NOR degradation with MFC0.1@ZnO as the photocatalyst may be primarily influenced by the following species, listed in decreasing order of importance: $O_2^{\bullet-} > HO^{\bullet} > h^+ > e^-$.

3.10. Reaction mechanism

The energy band edge positions of photocatalytic materials are crucial for the generation of reactive oxygen species (ROS) (Wang et al.,

Table 1
Photocatalytic performance of semiconductor oxide photocatalysts immobilized on carbon substrates for NOR degradation.

Materials	Light intensity	$[NOR]_0$	Dosage	Degradation efficiency	Time (min)	$k{\cdot}10^{-2}$ (min^{-1})	Ref.
ZnSe@rGO	100 mW cm^{-2}, simulated solar light	10 mg/L	1.0 mg/mL	83.5 %, pH = 7	40	5.7	Ghosh et al. (2023)
ZnS@rGO	300 W Hg vapor lamp, simulated solar light	20 mg/L	1.0 mg/mL	92 %, pH = 7	240	2.20	Bai et al. (2017)
Graphene/TiO_2-0.86%	300 W xenon lamp, simulated solar light	20 mg/L	1.0 mg/mL	86.2 %, pH = n/a	120	7.78	Li et al. (2013)
N–TiO_2/graphene	250 W mercury lamp, UV-A lamp	30 mg/L	n/a	50.0 %, pH = n/a	160	0.52	Zhao et al. (2020)
ZnO:$Ti_3C_2T_x$ = 1:1@ chitosan/polyacrylic	300 W xenon lamp, simulated solar light	20 mg/L	2.0 mg/mL	90 %, pH = 7	240	1.2	Chen et al. (2024)
CuO@Chitosan	Sun light	25 mg/L	0.8 mg/mL	71.9 %, pH = n/a	60	0.13	Ganeshbabu et al. (2023)
ZnO/ZnS@biochar	UV lamp	25 mg/L	0.5 mg/mL	55 %, pH = 7	180	2.12	Liu et al. (2020)
Biochar/A/R–TiO_2(550)	300 W xenon lamp, simulated solar light	50 mg/L	0.40 mg/mL	82.2 %, pH = n/a	120	1.44	An et al. (2023)
Carbon microspheres/BiOCl	500 W xenon lamp, simulated solar light	10 mg/L	0.50 mg/mL	36.0 %, pH = n/a	60	n/a	Zhao et al. (2022)
$CoFe_2O_4$@TiO_2@molecularly imprinted polymers	10 W UV-C lamp,	2 mg/L	0.40 mg/mL	84.2 %, pH = 7	150	7.5	Fang et al. (2023)
10% Ag–TiO_2/poly (vinylidene fluoride-co-hexafluoropropylene)	8 W UV-A lamp	5 mg/L	n/a	64.2 %, pH = n/a	90	1.1	Salazar et al. (2020)
20% Au–TiO_2/PVDF-HFP	8 W UV-A lamp	5 mg/L	n/a	72.0 %, pH = n/a	120	1.1	Martins et al. (2022)
MFC0.1@ZnO	300 W lamp, simulated solar light	5 mg/L	0.25 mg/mL	94,3 %, pH = 7.6	40	7.14	This work

2024). The valence band (VB) and conduction band (CB) edge positions of MFC0.1@ZnO can be estimated using the following equations:

$$E_{VB} = \chi - E_e + 0.5E_g \quad \text{Eq. 06}$$

$$E_{CB} = E_{VB} - E_g \quad \text{Eq. 07}$$

where E_e is the free electron energy based on the standard hydrogen electrode potential (E_e = 4.5 eV), E_g is the band gap energy estimated by the Tauc plot, and χ is the absolute electronegativity of ZnO (χ_{ZnO} = 5.79 eV) (Ayu et al., 2023). The CB and VB edges of this photocatalyst were found to be −0.36 eV and 2.94 eV, respectively.

The NOR photocatalytic degradation can be understood in three distinct stages. In the first, the NOR adsorption occurs on the ZnO NPs immobilized on microfibrillated cellulose. The high surface area displayed by MFC0.1–0.4@ZnO composite materials enable the adsorption of many NOR molecules, thus accelerating the degradation process.

The second stage involves photoexcited electrons and hole generation. When semiconductors are excited by photons with energy equal to or greater than their band gap, photoexcited electrons (e^-) and holes (h^+) are generated. Electrons at the VB position can migrate towards the CB positions of the catalysts, resulting in h^+ formation in the VB, which can directly oxidize NOR (Gao et al., 2023).

Due to the reduced size of the particles, both photoelectrons and holes show a higher probability of remaining confined to the particle surface, reducing electron-hole pair recombination (Kumar et al., 2019). Due to the shortening of the diffusion path of charge carriers to the material's surface, nanosizing hinders recombination (Xiao et al., 2020). Since MFC0.1@ZnO exhibited high efficiency even after cycling, it is suggested that recombination was minimized in this case.

The third stage is ROS formation, such as $HO^\bullet$ and $O_2^{\bullet-}$. The VB energy level of MFC0.1@ZnO (E_{VB} = 2.94 eV) is higher than the HO^- redox potential (+2.33 eV *vs.* NHE), facilitating $HO^\bullet$ formation, while the CB energy level is lower than the $O_2/O_2^{\bullet-}$ redox potential (−0.33 eV vs. NHE), allowing excess electrons to form $O_2^{\bullet-}$ radicals due to its more negative CB edge potential (E_{CB} = −0.36 eV *vs.* NHE) (Leite et al., 2024). The formation of ROS for NOR degradation is illustrated in Fig. 5b. As the $HO^\bullet$ and $O_2^{\bullet-}$ formation occurs simultaneously, efficient pollutant degradation has been related to the photocatalytic mechanism mediated by both (Silva et al., 2023). Furthermore, scavenger experiments support the idea that $HO^\bullet$ and $O_2^{\bullet-}$ are the main reactive species responsible for NOR degradation. The $HO^\bullet$ and $O_2^{\bullet-}$ species act as oxidizing agents (Lu et al., 2023), breaking the NOR molecule bonds into smaller units, whose TP degradation was investigated by LC-MS. The main reactions involved in NOR degradation can be summarized as follows:

$$NOR + MFC@ZnO \rightarrow NOR(ads) + MFC@ZnO \quad R6$$
$$MFC@ZnO + h\nu \rightarrow MFC@ZnO(e^-_{CB}) + MFC@ZnO(h^+_{VB}) \quad R7$$
$$MFC@ZnO(h^+) + OH^- \rightarrow MFC@ZnO + HO^\bullet \quad R8$$
$$MFC@ZnO(e^-_{CB}) + O_2 \rightarrow MFC@ZnO + O_2^{\bullet-} \quad R9$$

$$NOR + O_2^{\bullet-} + HO^\bullet + h^+ \rightarrow \text{Transformation products (TP)} \quad R10$$

3.11. Transformation products

The structures of the TP were based on fragmentation patterns obtained from LC/MS analysis (Figs. S3–S11) and information from previous studies (Chen and Chu, 2015; Ding et al., 2017; Carneiro et al., 2020). As summarized in Table S1, experiments conducted under UV-A and UV-C irradiation yielded seven main TP, whereas nine compounds were identified under SSL irradiation. This variation can be attributed to the higher photon flux of the solar system in solution, which leads to an increase in the concentration of reactive oxidant species, thereby enhancing the degradation of NOR molecule. The identified TP showed the NOR photodegradation pathways under the three different radiations (UV-A, UV-C, and SSL) that occur through the same four mechanisms of attack by oxidizing radicals (Fig. 5c).

The NOR degradation by the radicals on piperazinyl moieties was a main route that was observed (Pathway 1, **P1**), generating five of the nine TP identified. **DP 2** (*m/z* 349.31) and **DP 7** (*m/z* 354.31) were the primary TP, both obtained from the hydroxylation at the 2 and 3-carbon positions of the piperazine ring. In DP 2, the defluorination is due to the addition of a hydroxyl unit, following the loss of the NH_2 moiety, and the generation of an amide. In DP 7, the hydroxyl reaction induced decarbonylation in the amide of the piperazinyl ring, as previously reported in an NOR electrochemical degradation (Carneiro et al., 2020). The two hydroxyl groups removal from DP 7 through conversion into water during the oxidation, followed by structural rearrangement and the generation of an amide, gave rise to **DP 3** with *m/z* 322.31. In

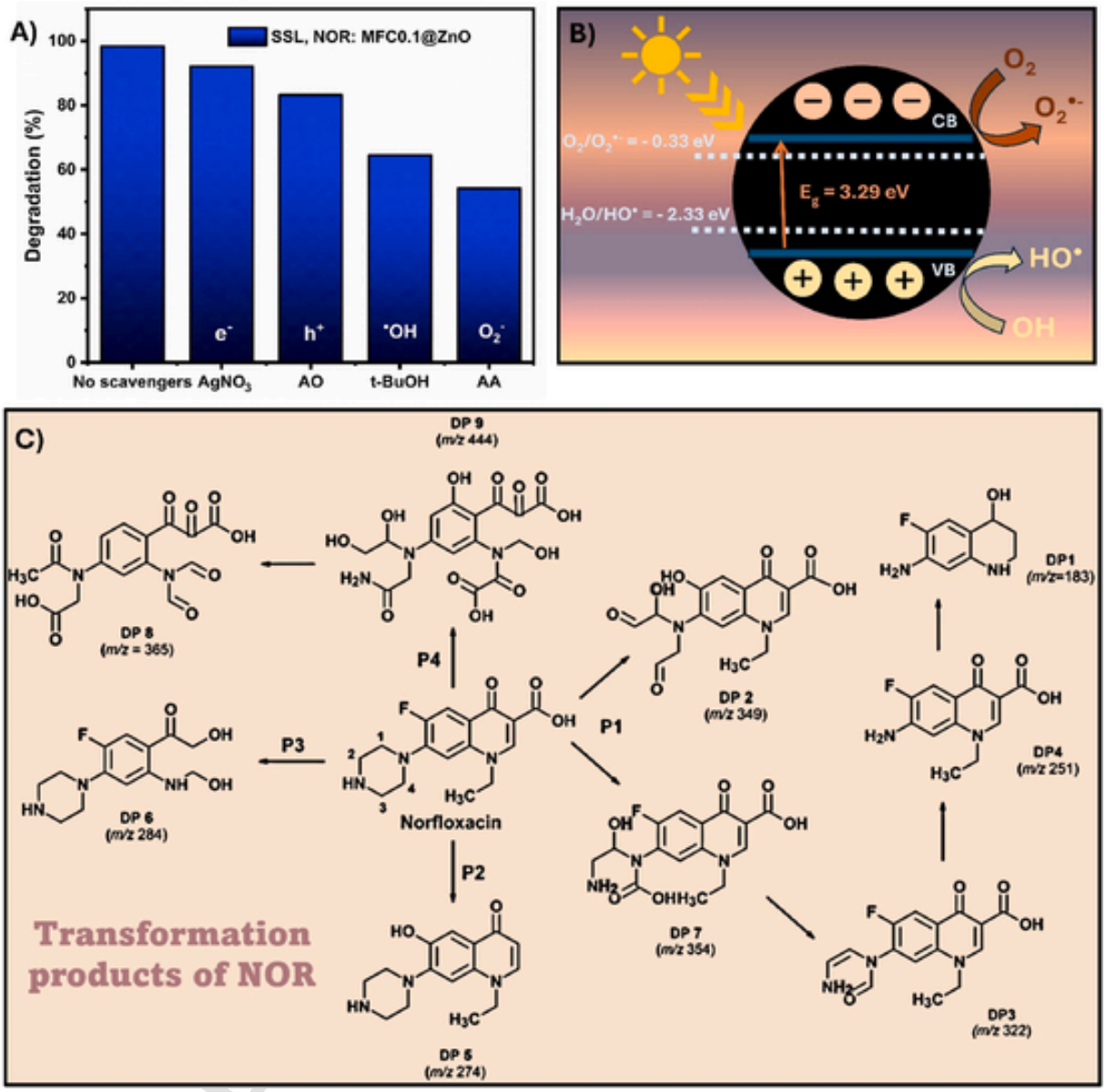

Fig. 5. (a) Radical-trapping experiments with different scavengers, (b) photocatalytic mechanism, and (c) presumptive proposal for degradation pathways of NOR using MFC0.1@ZnO as a photocatalyst under simulated solar light. (C_O = 5 mg L^{-1} NOR, photocatalytic dosage = 0.25 g L^{-1}, pH = 7.6, and 25 °C).

DP 3, the loss of the amine functional group (R–NH_2) and carbonyl group oxidation, resulting in the loss of C═O, led to TP **DP 4** at *m/z* 251.23. A similar reaction pathway and TP equivalent to the compounds with *m/z* 332 and 251 were reported in Bi_2WO_6 photocatalysis (Chen and Chu, 2015). Moreover, the high efficiency of the solar system converted DP 4 into a small molecular species with *m/z* 183.20 (**DP 1**). A comparable structure of DP 1 has been documented in the NOR photocatalytic Fenton-like degradation (Liu et al., 2022).

Pathway 2 (**P2**) was characterized by reactions involving both the addition and elimination of functional groups with no transformation of quinolone and piperazinyl rings. As reported in a previous study, the **DP 5** production with the protonated form at *m/z* 274.34 probably resulted from defluorination (−20 Da, corresponding to the loss of HF), decarboxylation (−44 Da, loss of CO_2), and hydroxylation (+16 Da, addition of OH^-) reactions (Ding et al., 2017). As depicted in Pathway 3 (**P3**), the attack of oxidizing radicals occurs on the alkene moiety of the quinolone ring. The cleavage of the C═C bond, leading to the ring opening, followed by decarboxylation and oxidation reactions with the C_2H_6 unit elimination, gave rise to **DP 6** (*m/z* 284.31).

In Pathway 4 (**P4**), as depicted in the structures of TP **DP 8** (*m/z* 365.27) and **DP 9** (*m/z* 444.32), the simultaneous attack of oxidizing agents occurs on quinolone and piperazine rings. In TP DP 9, it leads to the opening, hydroxylation, and oxidation of both rings of NOR, along with defluorination. DP 8 is suggested to be formed from DP 9 through several steps, including oxidation of the quinolone and piperazine rings, decarboxylation, substitution of the –NH_2 group by –OH, and release of a hydroxyl unit in the form of water.

3.12. Phytotoxicity assays

The phytotoxicity results using *C. sativus* exposed to NOR-degraded solutions are shown in Fig. 6a. It was observed that there was no significant variation in the root growth rate (RGI) for the photodegraded samples; however, the NOR sample exhibited an average RGI of 67%, repre-

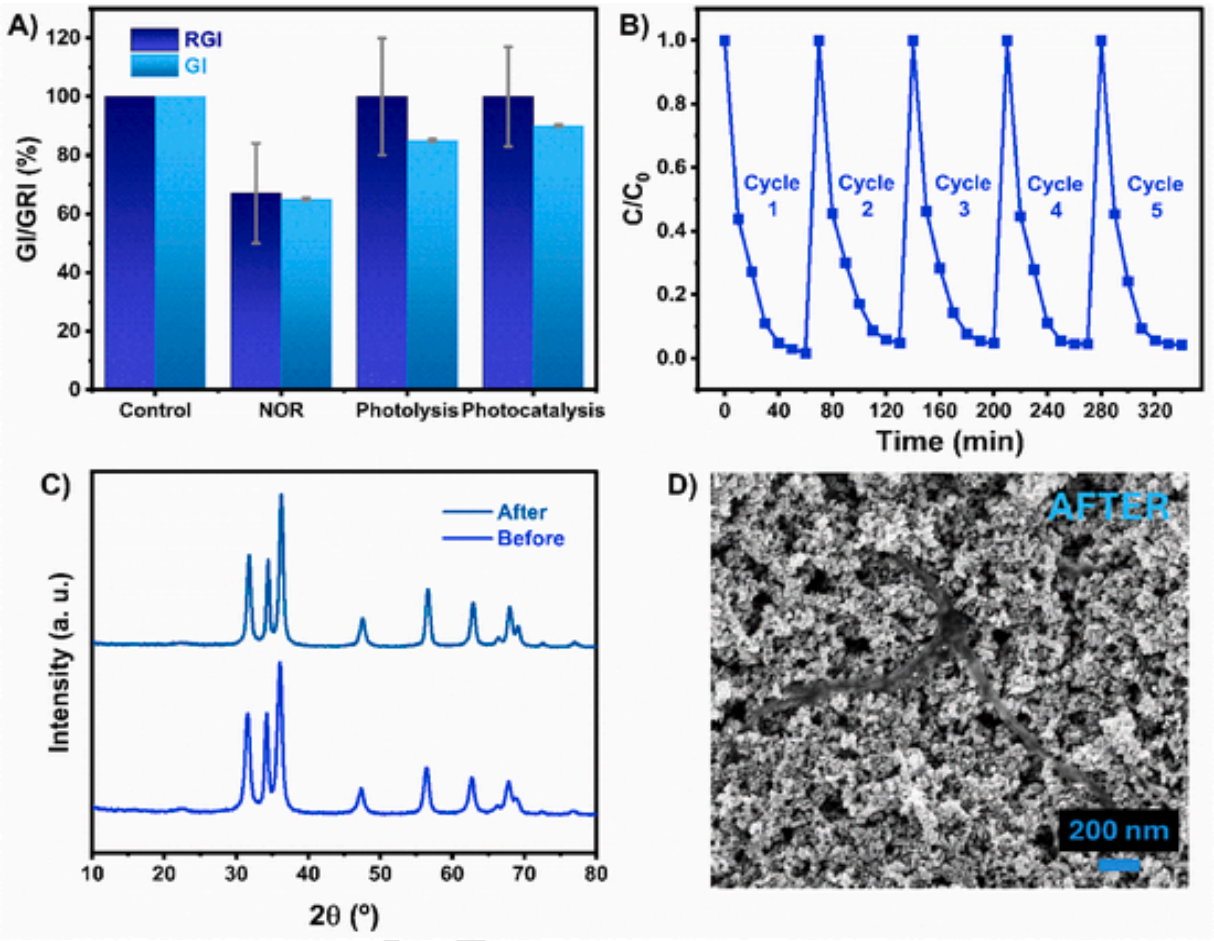

Fig. 6. (a) Phytotoxicity evaluation using the germination index (GI) and root growth index (GRI) of *Cucumis sativus* as a model for the photolysis and photodegradation products. (b) Reusability test for NOR degradation under simulated solar light using MFC0.1@ZnO as a photocatalyst. (c) Structural stability assessment by XRD. (d) Post-photocatalysis morphological characterization by FESEM.

senting a 33% decrease compared to the other samples. Additionally, the NOR sample had the lowest average germination index (GI = 65%), indicating that NOR negatively impacts growth and germination, suggesting potential toxicity. In contrast, photolysis and photocatalysis yielded average GI values of 85% and 90%, respectively, demonstrating that the photodegradation process reduced the sample's toxicity. The samples treated with photolytic and photocatalytic degradation using MFC0.1@ZnO showed no significant difference compared to the control. Therefore, it can be stated that the toxicity of the sample is reduced after the different photodegradation processes.

As toxicity may also be associated with the leaching of Zn^{2+} during the photocatalytic application stage, as reported in the literature (Silva et al., 2023; Marques et al., 2024), Zn^{2+} quantification by flame atomic absorption spectroscopy (FAAS) was performed. An analysis of the sample after 2 h of photocatalysis found Zn^{2+} = 5.73 mg L^{-1}, representing a 3% leaching with the amounts of catalyst (12.5 mg) and solution (50 mL) applied in the degradation assays. Different studies reported that at these concentrations, Zn^{2+} toxicity is not relevant for certain living organisms (Gebara et al., 2024; Marques et al., 2024). Thus, the Zn^{2+} leaching of only 3% after 2 h of photocatalysis confirms the good stability of the material during the application.

3.13. Evaluation of MFC0.1@ZnO reusability

Fig. 6b illustrates the reusability of photocatalyst MFC0.1@ZnO for the photocatalytic degradation of NOR under simulated sunlight. The nanocomposite maintained its excellent photocatalytic performance, with a slight reduction in efficiency from 98.4% to 95.8% after five 60-min cycles. This stability is attributed to the hierarchical porous network structure derived from cellulose (Lin et al., 2019), and the slight 2.6% decrease in degradation efficiency may be due to mass loss during the photocatalyst recovery. Post-photocatalysis characterization of the photocatalyst by XRD (Fig. 6c) and FEG-SEM (Fig. 6d) suggests that MFC0.1@ZnO retained its structural and morphological stability, respectively. No changes in crystal structure or morphology were observed after the photocatalytic experiment. Moreover, the maintenance of structural and morphological stability after photocatalysis reinforces the viability of MFC0.1@ZnO as a robust and reliable option for emergent pollutant degradation, ensuring that the material can be reused without significant loss of performance. This resistance to structural and morphological changes not only ensures the ongoing effectiveness of the photocatalyst but also highlights its potential for applications in water and wastewater treatment, where material durability and robustness are crucial for long-term success.

4. Conclusions

For the first time, *in situ* immobilization of ZnO nanoparticles on cellulosic materials was developed for the photocatalytic degradation of the antibiotic norfloxacin. Composites of MFC0.1–0.4@ZnO, synthesized with varying concentrations of MFC suspensions, exhibited small particle sizes and high surface areas (~50 m^2/g), which are beneficial

for enhancing photocatalytic performance. Notably, increasing the concentration of MFC suspension did not result in significant improvements in photocatalytic efficiency for degrading NOR. Experiments conducted under different radiation sources, including UV-A, UV-C, and SSL, demonstrated excellent performance across all types of irradiations, achieving efficiencies exceeding 94% after 60 min. Additionally, a minimal efficiency loss of only 3% was observed after five cycles of photocatalyst reuse. The high performance of the photocatalyst in degrading NOR under various conditions underscores its potential for effectively treating effluents containing this molecule with minimal pre-treatment adjustments. This suggests that the material can be utilized across a range of concentrations, doses, and pH levels. The optimal conditions for the photocatalyst were determined to be a concentration of 0.25 g L^{-1} of MFC0.1@ZnO, a NOR concentration of 5 mg L^{-1}, and a degradation pH of around 8. The results highlight the potential of MFC0.1–0.4@ZnO composites as an effective and sustainable approach for removing emerging pollutants from contaminated environments.

CRediT authorship contribution statement

Ramon Resende Leite: Writing – review & editing, Writing – original draft, Visualization, Methodology, Investigation, Formal analysis, Conceptualization. **Renata Colombo:** Writing – review & editing, Writing – original draft, Visualization, Validation, Methodology, Investigation, Formal analysis. **Ailton José Moreira:** Writing – review & editing, Visualization, Methodology, Investigation, Formal analysis. **Júlia Mendes Farias:** Methodology, Investigation. **Fausto Eduardo Bimbi Júnior:** Writing – review & editing, Methodology, Investigation. **Juliana Bruzaca Lima:** Writing – review & editing, Methodology, Investigation, Formal analysis. **Marcos Roberto de Vasconcelos Lanza:** Writing – review & editing, Resources, Funding acquisition. **Hernane da Silva Barud:** Writing – review & editing. **Maria Inês Basso Bernardi:** Writing – review & editing, Supervision, Project administration, Funding acquisition.

Declaration of competing interest

The authors declare that they have no known competing financial interests or personal relationships that could have appeared to influence the work reported in this paper.

Data availability

Data will be made available on request.

Appendix A. Supplementary data

Supplementary data to this article can be found online at https://doi.org/10.1016/j.chemosphere.2024.143888.

References

Agarwal, S., Jangir, L.K., Rathore, K.S., Kumar, M., Awasthi, K., 2019. Morphology-dependent structural and optical properties of ZnO nanostructures. Appl. Phys. A 125, 553. https://doi.org/10.1007/s00339-019-2852-x.

AL Falahi, O.A., Abdullah, S.R.S., Hasan, H.A., Othman, A.R., Ewadh, H.M., Kurniawan, S.B., Imron, M.F., 2022. Occurrence of pharmaceuticals and personal care products in domestic wastewater, available treatment technologies, and potential treatment using constructed wetland: a review. Process Saf. Environ. Protect. 168, 1067–1088. https://doi.org/10.1016/j.psep.2022.10.082.

An, M., Yang, Z., Zhang, B., Xue, B., Xu, G., Chen, W., Wang, S., 2023. Construction of biochar-modified TiO_2 anatase-rutile phase S-scheme heterojunction for enhanced performance of photocatalytic degradation and photocatalytic hydrogen evolution. J. Environ. Chem. Eng. 11, 110367. https://doi.org/10.1016/j.jece.2023.110367.

Anirudhan, T.S., Deepa, J.R., 2017. Nano-zinc oxide incorporated graphene oxide/nanocellulose composite for the adsorption and photo catalytic degradation of ciprofloxacin hydrochloride from aqueous solutions. J. Colloid Interface Sci. 490, 343–356. https://doi.org/10.1016/j.jcis.2016.11.042.

Arakha, M., Roy, J., Nayak, P.S., Mallick, B., Jha, S., 2017. Zinc oxide nanoparticle energy band gap reduction triggers the oxidative stress resulting into autophagy-mediated apoptotic cell death. Free Radic. Biol. Med. 110, 42–53. https://doi.org/10.1016/j.freeradbiomed.2017.05.015.

Ayu, D.G., Gea, S., Andriayani, Telaumbanua, D.J., Piliang, A.F.R., Harahap, M., Yen, Z., Goei, R., Tok, A.I.Y., 2023. Photocatalytic degradation of methylene blue using N-doped ZnO/carbon dot (N-ZnO/CD) nanocomposites derived from organic soybean. ACS Omega 8, 14965–14984. https://doi.org/10.1021/acsomega.2c07546.

Bai, J., Li, Y., Jin, P., Wang, J., Liu, L., 2017. Facile preparation 3D ZnS nanospheres-reduced graphene oxide composites for enhanced photodegradation of norfloxacin. J. Alloys Compd. 729, 809–815. https://doi.org/10.1016/j.jallcom.2017.07.057.

Bano, K., Kaushal, S., Lal, B., Joshi, S.K., Kumar, R., Singh, P.P., 2023. Fabrication of CuO/ZnO heterojunction photocatalyst for efficient photocatalytic degradation of tetracycline and ciprofloxacin under direct sun light. Environ. Nanotechnol. Monit. Manag. 20, 100863. https://doi.org/10.1016/j.enmm.2023.100863.

Carneiro, J.F., Aquino, J.M., Silva, B.F., Silva, A.J., Rocha-Filho, R.C., 2020. Comparing the electrochemical degradation of the fluoroquinolone antibiotics norfloxacin and ciprofloxacin using distinct electrolytes and a BDD anode: evolution of main oxidation byproducts and toxicity. J. Environ. Chem. Eng. 8, 104433. https://doi.org/10.1016/j.jece.2020.104433.

Chen, J., Liu, F., Abdiryim, T., Yin, H., Liu, X., 2024. ZnO-Ti_3C_2TX composites supported on polyacrylic acid/chitosan hydrogels as high-efficiency and recyclable photocatalysts for norfloxacin degradation. Int. J. Biol. Macromol. 258, 128912. https://doi.org/10.1016/j.ijbiomac.2023.128912.

Chen, M., Chu, W., 2015. Photocatalytic degradation and decomposition mechanism of fluoroquinolones norfloxacin over bismuth tungstate: experiment and mathematic model. Appl. Catal. B Environ. 168–169, 175–182. https://doi.org/10.1016/j.apcatb.2014.12.023.

Chen, X., Zhuan, R., Wang, J., 2021. Assessment of degradation characteristic and mineralization efficiency of norfloxacin by ionizing radiation combined with Fenton-like oxidation. J. Hazard Mater. 404, 124172. https://doi.org/10.1016/j.jhazmat.2020.124172.

Chen, Y., Li, C., Zhang, L., Chen, Q., Zhang, S., Xiang, J., Hu, S., Wang, Y., Hu, X., 2023. Interaction of the lignin-/cellulose-derived char with volatiles of varied origin: Part of the process for evolution of products in pyrolysis. Chemosphere 336, 139248. https://doi.org/10.1016/j.chemosphere.2023.139248.

Das, R., Lindström, T., Sharma, P.R., Chi, K., Hsiao, B.S., 2022. Nanocellulose for sustainable water purification. Chem. Rev. 122, 8936–9031. https://doi.org/10.1021/acs.chemrev.1c00683.

Dehghani, M., Nadeem, H., Singh Raghuwanshi, V., Mahdavi, H., Banaszak Holl, M.M., Batchelor, W., 2020. ZnO/Cellulose nanofiber composites for sustainable sunlight-driven dye degradation. ACS Appl. Nano Mater. 3, 10284–10295. https://doi.org/10.1021/acsanm.0c02199.

Ding, D., Liu, C., Ji, Y., Yang, Q., Chen, L., Jiang, C., Cai, T., 2017. Mechanism insight of degradation of norfloxacin by magnetite nanoparticles activated persulfate: identification of radicals and degradation pathway. Chem. Eng. J. 308, 330–339. https://doi.org/10.1016/j.cej.2016.09.077.

Du, M., Du, Y., Feng, Y., Yang, K., Lv, X., Jiang, N., Liu, Y., 2018. Facile preparation of BiOBr/cellulose composites by in situ synthesis and its enhanced photocatalytic activity under visible-light. Carbohydr. Polym. 195, 393–400. https://doi.org/10.1016/j.carbpol.2018.04.092.

El Golli, A., Fendrich, M., Bazzanella, N., Dridi, C., Miotello, A., Orlandi, M., 2021. Wastewater remediation with ZnO photocatalysts: green synthesis and solar concentration as an economically and environmentally viable route to application. J. Environ. Manag. 286, 112226. https://doi.org/10.1016/j.jenvman.2021.112226.

Fang, L., Tang, K., Wei, D., Zhang, Y., Zhou, Y., 2023. Photocatalytic degradation of norfloxacin by magnetic molecularly imprinted polymers: influencing factors and mechanisms. Environ. Technol. 44, 1438–1449. https://doi.org/10.1080/09593330.2021.2003442.

Fu, F., Gu, J., Xu, X., Xiong, Q., Zhang, Y., Liu, X., Zhou, J., 2017. Interfacial assembly of ZnO–cellulose nanocomposite films via a solution process: a one-step biomimetic approach and excellent photocatalytic properties. Cellulose 24, 147–162. https://doi.org/10.1007/s10570-016-1087-7.

Ganeshbabu, M., Priya, J.S., Manoj, G.M., Puneeth, N.P.N., Shobana, C., Shankar, H., Selvan, R.K., 2023. Photocatalytic degradation of fluoroquinolone antibiotics using chitosan biopolymer functionalized copper oxide nanoparticles prepared by facile sonochemical method. Int. J. Biol. Macromol. 253, 127027. https://doi.org/10.1016/j.ijbiomac.2023.127027.

Gao, W., Wang, F., Ou, M., Wu, Q., Wang, L., Zhu, H., Li, Y., Kong, N., Qiu, J., Hu, S., Song, S., 2023. Enhancing degradation of norfloxacin using chrysanthemum-shaped bimetallic NH_2-MIL-53(Fe/Ti) photocatalysts under visible light irradiation. J. Environ. Chem. Eng. 11, 111050. https://doi.org/10.1016/j.jece.2023.111050.

Gebara, R.C., Abreu, C.B. de, Rocha, G.S., Mansano, A. da S., Assis, M., Moreira, A.J., Santos, M.A., Pereira, T.M., Virtuoso, L.S., Melão, M. da G.G., Longo, E., 2024. Effects of $ZnWO_4$ nanoparticles on growth, photosynthesis, and biochemical parameters of the green microalga Raphidocelis subcapitata. Chemosphere 353, 141590. https://doi.org/10.1016/j.chemosphere.2024.141590.

Ghosh, S., Kar, S., Pal, T., Ghosh, S., 2023. Sunlight-driven photocatalytic degradation of Norfloxacin antibiotic in wastewater by ZnSe microsphere functionalized RGO composite. Sustain. Chem. Environ. 4, 100038. https://doi.org/10.1016/j.scenv.2023.100038.

Hoogendoorn, B.W., Birdsong, B.K., Capezza, A.J., Ström, V., Li, Y., Xiao, X., Olsson, R.T., 2022. Ultra-low concentration of cellulose nanofibers (CNFs) for enhanced nucleation and yield of ZnO nanoparticles. Langmuir 38, 12480–12490. https://doi.org/10.1021/acs.langmuir.2c01713.

Janpetch, N., Saito, N., Rujiravanit, R., 2016. Fabrication of bacterial cellulose-ZnO composite via solution plasma process for antibacterial applications. Carbohydr. Polym. 148, 335–344. https://doi.org/10.1016/j.carbpol.2016.04.066.

Jing, R., Ibni Khursheed, A., Song, J., Sun, L., Yu, Z., Nie, Z., Cao, E., 2022. A comparative study on the acetone sensing properties of ZnO disk pairs, flowers, and walnuts prepared by hydrothermal method. Appl. Surf. Sci. 591, 153218. https://doi.org/10.1016/j.apsusc.2022.153218.

Kamal Mohamed, S.M., Ganesan, K., Milow, B., Ratke, L., 2015. The effect of zinc oxide (ZnO) addition on the physical and morphological properties of cellulose aerogel beads. RSC Adv. 5, 90193–90201. https://doi.org/10.1039/C5RA17366C.

Kar, S., Pal, T., Ghosh, S., 2023. Removal of norfloxacin from wastewater by adsorption onto SnS_2 followed by photocatalytic degradation. ChemistrySelect 8. https://doi.org/10.1002/slct.202300878.

Ko, H.-U., Mun, S., Min, S.-K., Kim, G.-W., Kim, J., 2014. Fabrication of cellulose ZnO hybrid nanocomposite and its strain sensing behavior. Materials 7, 7000–7009. https://doi.org/10.3390/ma7107000.

Kumar, V., Choudhary, S., Malik, V., Nagarajan, R., Kandasami, A., Subramanian, A., 2019. Enhancement in photocatalytic activity of $SrTiO_3$ by tailoring particle size and defects. Phys. Status Solidi 216. https://doi.org/10.1002/pssa.201900294.

Leite, R.R., Colombo, R., Eduardo Bimbi Júnior, F., Roberto de Vasconcelos Lanza, M., da Silva Barud, H., Ramos Moreira Afonso, C., Inês Basso Bernardi, M., 2024. Precursor effect on the hydrothermal synthesis of pure ZnO nanostructures and enhanced photocatalytic performance for norfloxacin degradation. Chem. Eng. J. 496, 154374. https://doi.org/10.1016/j.cej.2024.154374.

Li, K., Xiong, J., Chen, T., Yan, L., Dai, Y., Song, D., Lv, Y., Zeng, Z., 2013. Preparation of graphene/TiO_2 composites by nonionic surfactant strategy and their simulated sunlight and visible light photocatalytic activity towards representative aqueous POPs degradation. J. Hazard Mater. 250–251, 19–28. https://doi.org/10.1016/j.jhazmat.2013.01.069.

Li, X., Chen, H., Zhang, L., Wang, Z., Wu, S., Ma, J., 2023. The interface design and properties enhancement of ZnO/cellulose composites: branching fiber network to guide the assembly of ZnO flower. J. Colloid Interface Sci. 641, 539–552. https://doi.org/10.1016/j.jcis.2023.03.096.

Li, X., Li, H., Wang, X., Xu, D., You, T., Wu, Y., Xu, F., 2021a. Facile in situ fabrication of ZnO-embedded cellulose nanocomposite films with antibacterial properties and enhanced mechanical strength via hydrogen bonding interactions. Int. J. Biol. Macromol. 183, 760–771. https://doi.org/10.1016/j.ijbiomac.2021.04.175.

Li, X., Zhang, L., Wang, Z., Wu, S., Ma, J., 2022. Facile fabrication of multiscale ZnO/cellulose composite membrane towards enhancing photocatalytic and mechanical properties. Colloids Surfaces A Physicochem. Eng. Asp. 636, 128156. https://doi.org/10.1016/j.colsurfa.2021.128156.

Li, X., Zhang, L., Wang, Z., Wu, S., Ma, J., 2021b. Cellulose controlled zinc oxide nanoparticles with adjustable morphology and their photocatalytic performances. Carbohydr. Polym. 259, 117752. https://doi.org/10.1016/j.carbpol.2021.117752.

Li, Y., Sun, H., Zhang, Y., Xu, M., Shi, S.Q., 2019. The three-dimensional heterostructure synthesis of ZnO/cellulosic fibers and its application for rubber composites. Compos. Sci. Technol. 177, 10–17. https://doi.org/10.1016/j.compscitech.2019.04.012.

Lima, A.E.B., Reis, R.Y.N., Ribeiro, L.S., Ribeiro, L.K., Assis, M., Santos, R.S., Fernandes, C.H.M., Cavalcante, L.S., Longo, E., Osajima, J.A.O., Luz, G.E., 2021. Microwave-assisted hydrothermal synthesis of $CuWO_4$-palygorskite nanocomposite for enhanced visible photocatalytic response. J. Alloys Compd. 863, 158731. https://doi.org/10.1016/j.jallcom.2021.158731.

Lin, Z., Lu, Y., Huang, J., 2019. A hierarchical Ag_2O-nanoparticle/TiO_2-nanotube composite derived from natural cellulose substance with enhanced photocatalytic performance. Cellulose 26, 6683–6700. https://doi.org/10.1007/s10570-019-02573-z.

Liu, W., He, T., Wang, Y., Ning, G., Xu, Z., Chen, X., Hu, X., Wu, Y., Zhao, Y., 2020. Synergistic adsorption-photocatalytic degradation effect and norfloxacin mechanism of ZnO/ZnS@BC under UV-light irradiation. Sci. Rep. 10, 11903. https://doi.org/10.1038/s41598-020-68517-x.

Liu, Y., Wang, X., Ye, W., Butenko, D.S., Lu, P., Chen, Q., Cai, R., Sun, J., Zhu, Y., Yang, D., 2022. FeOx nanoclusters decorated TiO_2 for boosting white LED driven photocatalytic Fenton-like norfloxacin degradation. Sep. Purif. Technol. 303, 122194. https://doi.org/10.1016/j.seppur.2022.122194.

Lu, Y., Chen, R., Wu, F., Gan, W., Zhao, Z., Chen, L., Zhang, M., Sun, Z., 2023. A novel SiP/TiO_2 S-scheme heterojunction photocatalyst for efficient degradation of norfloxacin. Sep. Purif. Technol. 324, 124572. https://doi.org/10.1016/j.seppur.2023.124572.

Malekkiani, M., Heshmati Jannat Magham, A., Ravari, F., Dadmehr, M., 2022. Facile fabrication of ternary MWCNTs/ZnO/Chitosan nanocomposite for enhanced photocatalytic degradation of methylene blue and antibacterial activity. Sci. Rep. 12, 5927. https://doi.org/10.1038/s41598-022-09571-5.

Manasa, M., Chandewar, P.R., Mahalingam, H., 2021. Photocatalytic degradation of ciprofloxacin & norfloxacin and disinfection studies under solar light using boron & cerium doped TiO_2 catalysts synthesized by green EDTA-citrate method Catal. Today Off. 375, 522–536. https://doi.org/10.1016/j.cattod.2020.03.018.

Marques, G.N., Moreira, A.J., Nóbrega, E.T.D., Braga, S., Argentin, M.N., da Cunha Camargo, I.L.B., Azevedo, E., Pereira, E.C., Bernardi, M.I.B., Mascaro, L.H., 2024. Selective inhibitory activity of multidrug-resistant bacteria by zinc oxide nanoparticles. J. Environ. Chem. Eng. 12, 111870. https://doi.org/10.1016/j.jece.2023.111870.

Martins, P.M., Santos, B., Salazar, H., Carabineiro, S.A.C., Botelho, G., Tavares, C.J., Lanceros-Mendez, S., 2022. Multifunctional hybrid membranes for photocatalytic and adsorptive removal of water contaminants of emerging concern. Chemosphere 293, 133548. https://doi.org/10.1016/j.chemosphere.2022.133548.

Mohamed, M.A., W. Salleh, W.N., Jaafar, J., Mohd Hir, Z.A., Rosmi, M.S., Abd Mutalib, M., Ismail, A.F., Tanemura, M., 2016. Regenerated cellulose membrane as bio-template for in-situ growth of visible-light driven C-modified mesoporous titania. Carbohydr. Polym. 146, 166–173. https://doi.org/10.1016/j.carbpol.2016.03.050.

Montero-Muñoz, M., Ramos-Ibarra, J.E., Rodríguez-Páez, J.E., Teodoro, M.D., Marques, G.E., Sanabria, A.R., Cajas, P.C., Páez, C.A., Heinrichs, B., Coaquira, J.A.H., 2018. Role of defects on the enhancement of the photocatalytic response of ZnO nanostructures. Appl. Surf. Sci. 448, 646–654. https://doi.org/10.1016/j.apsusc.2018.04.105.

Nahi, J., Radhakrishnan, A., Beena, B., 2021. Green synthesis of zinc oxide incorporated nanocellulose with visible light photocatalytic activity and application for the removal of antibiotic enrofloxacin from aqueousmedia. Mater. Today Proc. 41, 583–589. https://doi.org/10.1016/j.matpr.2020.05.253.

Pinheiro, B.S., Moreira, A.J., Gimenes, L.L.S., Freschi, C.D., Freschi, G.P.G., 2020. UV photochemical hydride generation using ZnO nanoparticles for arsenic speciation in waters, sediments, and soils samples. Environ. Monit. Assess. 192, 331. https://doi.org/10.1007/s10661-020-08316-z.

Qiu, J., Li, M., Ding, M., Yao, J., 2022. Cellulose tailored semiconductors for advanced photocatalysis. Renew. Sustain. Energy Rev. 154, 111820. https://doi.org/10.1016/j.rser.2021.111820.

Resende Leite, R., Komorizono, A.A., Basso Bernardi, M.I., Carvalho, A.J.F., Mastelaro, V.R., 2024. Environmentally friendly synthesis of In_2O_3 nano octahedrons by cellulose nanofiber template-assisted route and their potential application for O_3 gas sensing. Ceram. Int. 50, 10192–10202. https://doi.org/10.1016/j.ceramint.2023.12.329.

Salazar, H., Martins, P.M., Santos, B., Fernandes, M.M., Reizabal, A., Sebastián, V., Botelho, G., Tavares, C.J., Vilas-Vilela, J.L., Lanceros-Mendez, S., 2020. Photocatalytic and antimicrobial multifunctional nanocomposite membranes for emerging pollutants water treatment applications. Chemosphere 250, 126299. https://doi.org/10.1016/j.chemosphere.2020.126299.

Shen, J.-H., Chiang, T.-H., Tsai, C.-K., Jiang, Z.-W., Horng, J.-J., 2022. Mechanistic insights into hydroxyl radical formation of Cu-doped ZnO/g-C_3N_4 composite photocatalysis for enhanced degradation of ciprofloxacin under visible light: efficiency, kinetics, products identification and toxicity evaluation. J. Environ. Chem. Eng. 10, 107352. https://doi.org/10.1016/j.jece.2022.107352.

Shi, C., An, B., Zhang, L., Zai, Z., Shi, Z., Wang, Z., Ma, J., 2023. Contribution of surface carboxyl of cellulose in the formation mechanism and interfacial catalysis activity of ZnO/cellulose nanocomposites. Appl. Surf. Sci. 618, 156633. https://doi.org/10.1016/j.apsusc.2023.156633.

Silva, T.E.M., Moreira, A.J., Nobrega, E.T.D., Alencar, R.G., Rabello, P.T., Blaskievicz, S.F., Marques, G.N., Mascaro, L.H., Paris, E.C., Lemos, S.G., Pereira, E.C., Freschi, G.P.G., 2023. Hierarchical structure of 3D ZnO experimentally designed to achieve high performance in the sertraline photocatalysis in natural waters. Chem. Eng. J. 475, 146235. https://doi.org/10.1016/j.cej.2023.146235.

Singh, R., Verma, K., Patyal, A., Sharma, I., Barman, P.B., Sharma, D., 2019. Nanosheet and nanosphere morphology dominated photocatalytic & antibacterial properties of ZnO nanostructures. Solid State Sci. 89, 1–14. https://doi.org/10.1016/j.solidstatesciences.2018.12.011.

Son, G.S., Yeo, J.-A., Kim, M.-S., Kim, S.K., Holmén, A., Åkerman, B., Nordén, B., 1998. Binding mode of norfloxacin to calf thymus DNA. J. Am. Chem. Soc. 120, 6451–6457. https://doi.org/10.1021/ja9734049.

Song, X., Zhuo, B., Cao, S., Huang, L., Zhu, Q., Zhang, J., Yuan, Q., 2024. High performance and flexible piezoelectric composite incorporating zinc oxide grown on the oxidized nanocellulose by two-step hydrothermal process. Appl. Surf. Sci. 649, 158996. https://doi.org/10.1016/j.apsusc.2023.158996.

Supramaniam, J., Low, D.Y.S., Wong, S.K., Tan, L.T.H., Leo, B.F., Goh, B.H., Darji, D., Rasdi, F.R.M., Chan, K.G., Lee, L.H., Tang, S.Y., 2021. Facile synthesis and characterization of palm CNF-ZnO nanocomposites with antibacterial and reinforcing properties. Int. J. Mol. Sci. 22. https://doi.org/10.3390/ijms22115781.

Tan, S., Li, J., Zhou, L., Chen, P., Xu, D., Xu, Z., 2018. Fabrication of a flexible film electrode based on cellulose nanofibers aerogel dispersed with functionalized graphene decorated with SnO_2 for supercapacitors. J. Mater. Sci. 53, 11648–11658. https://doi.org/10.1007/s10853-018-2413-2.

Tavker, N., Sharma, M., 2018. Enhanced photocatalytic activity of nanocellulose supported zinc oxide composite for RhB dye as well as ciprofloxacin drug under sunlight/visible light. https://doi.org/10.1063/1.5035215.

Vasistha, S., Balakrishnan, D., Manivannan, A., Rai, M.P., 2023. Microalgae on distillery wastewater treatment for improved biodiesel production and cellulose nanofiber synthesis: a sustainable biorefinery approach. Chemosphere 315, 137666. https://doi.org/10.1016/j.chemosphere.2022.137666.

Wang, N., Wang, W., Qi, D., Kang, G., Wang, B., Zhang, H., Ruan, J., Lei, R., Zhang, Z., Zhang, S., Zhou, H., 2024. Development of efficient and economic Bi_2O_3/BN/Co_3O_4 composite photocatalyst: degradation mechanism, pathway and toxicity study of norfloxacin. Chemosphere 352, 141481. https://doi.org/10.1016/j.chemosphere.2024.141481.

Xiao, H., Shan, Y., Zhang, W., Huang, L., Chen, L., Ni, Y., Boury, B., Wu, H., 2020. C-nanocoated ZnO by TEMPO-oxidized cellulose templating for improved photocatalytic performance. Carbohydr. Polym. 235, 115958. https://doi.org/10.1016/j.carbpol.2020.115958.

Xiao, H., Zhang, W., Wei, Y., Yu, L., Chen, L., 2018. Fabrication of Fe/ZnO composite nanosheets by nanofibrillated cellulose as soft template and photocatalytic degradation for tetracycline. J. Inorg. Organomet. Polym. Mater. 28, 1299–1304. https://doi.org/10.1007/s10904-017-0712-8.

Yan, M., An, B., Li, X., Zai, Z., Wu, S., Ma, J., Zhang, L., 2023a. Effect of different electronegative oxygen atoms of cellulose nanofibrils on the formation and photocatalytic property of ZnO/cellulose composite. Appl. Surf. Sci. 637, 157974. https://doi.org/10.1016/j.apsusc.2023.157974.

Yan, M., An, B., Zai, Z., Zhang, L., Li, X., Wu, S., Ma, J., 2023b. The mechanism of acetyl groups regulating the morphology and photocatalytic properties of ZnO and its cellulose composite. Cellulose 30, 6869–6885. https://doi.org/10.1007/s10570-023-

05344-z.
Yang, X., Zhang, X., Wang, Z., Li, S., Zhao, J., Liang, G., Xie, X., 2019. Mechanistic insights into removal of norfloxacin from water using different natural iron ore – biochar composites: more rich free radicals derived from natural pyrite-biochar composites than hematite-biochar composites. Appl. Catal. B Environ. 255, 117752. https://doi.org/10.1016/j.apcatb.2019.117752.
Yu, J., Bao, P., Liu, J., Jin, Y., Li, J., Lv, Y., 2023. Cu and Ni dual-doped ZnO nanostructures templated by cellulose nanofibrils for the boosted visible-light photocatalytic degradation of wastewater pollutants. Green Chem. 25, 10530–10537. https://doi.org/10.1039/D3GC04163H.
Zhang, Y., Zhao, G., Xuan, Y., Gan, L., Pan, M., 2021. Enhanced photocatalytic performance for phenol degradation using ZnO modified with nano-biochar derived from cellulose nanocrystals. Cellulose 28, 991–1009. https://doi.org/10.1007/s10570-020-03581-0.
Zhao, M., Yang, Y., Zha, Z., Cui, S., Li, Y., Yang, J., 2022. Enhanced photocatalytic performance of layered carbon microsphere/BiOCl composite with oxygen vacancies. J. Alloys Compd. 928, 167068. https://doi.org/10.1016/j.jallcom.2022.167068.
Zhao, W., Duan, J., Ji, B., Ma, L., Yang, Z., 2020. Novel formation of large area N-TiO_2/graphene layered materials and enhanced photocatalytic degradation of antibiotics. J. Environ. Chem. Eng. 8, 102206. https://doi.org/10.1016/j.jece.2018.02.014.
Zhao, Z., Ling, Q., Li, Z., Yan, K., Ding, C., Chen, P., Yang, L., Sun, Z., Zhang, M., 2023. S-Scheme $BaTiO_3$/TiO_2 heterojunctions: piezophotocatalytic degradation of norfloxacin. Sep. Purif. Technol. 308, 122928. https://doi.org/10.1016/j.seppur.2022.122928.
Zhou, X., Li, X., Gao, Y., Li, L.C., Huang, L., Ye, J., 2019. Preparation and characterization of 2D ZnO nanosheets/regenerated cellulose photocatalytic composite thin films by a two-step synthesis method. Mater. Lett. 234, 26–29. https://doi.org/10.1016/j.matlet.2018.09.070.